nature energy

ARTICLES

https://doi.org/10.1038/s41560-021-00783-z

Check for updates

Tailoring electrolyte solvation for Li metal batteries cycled at ultra-low temperature

John Holoubek[1], Haodong Liu[1], Zhaohui Wu[3], Yijie Yin[2], Xing Xing[2], Guorui Cai[1], Sicen Yu[2], Hongyao Zhou[1], Tod A. Pascal[1,2,3,4] ✉, Zheng Chen[1,2,3,4] ✉ and Ping Liu[1,2,3,4] ✉

Lithium metal batteries hold promise for pushing cell-level energy densities beyond 300 Wh kg^{-1} while operating at ultra-low temperatures (below −30 °C). Batteries capable of both charging and discharging at these temperature extremes are highly desirable due to their inherent reduction in the need for external warming. Here we demonstrate that the local solvation structure of the electrolyte defines the charge-transfer behaviour at ultra-low temperature, which is crucial for achieving high Li metal Coulombic efficiency and avoiding dendritic growth. These insights were applied to Li metal full-cells, where a high-loading 3.5 mAh cm^{-2} sulfurized polyacrylonitrile (SPAN) cathode was paired with a onefold excess Li metal anode. The cell retained 84% and 76% of its room temperature capacity when cycled at −40 and −60 °C, respectively, which presented stable performance over 50 cycles. This work provides design criteria for ultra-low-temperature lithium metal battery electrolytes, and represents a defining step for the performance of low-temperature batteries.

The deployment of rechargeable lithium-ion batteries (LIB) is crucial to the operation of modern portable electronics in extreme environments, where a reduction in cell energy density at ultra-low temperatures (−30 °C and below) has limited operations in electric vehicles, subsea, military and defence devices, and space exploration[1–6]. In principle, this can be accomplished by both increasing the baseline energy density of the battery, or mitigating the energy loss at low temperatures via improvement of the charge-transfer kinetics. Intuitively, ideal performance would be produced by a system inherently capable of doing both of these things simultaneously.

To address the former of these improvements, replacing the commonly applied graphite anode (372 mAh g^{-1}) with Li metal (3,860 mAh g^{-1}) has been noted as an effective step to push cell energy densities above 300 Wh kg^{-1} (ref. [7]). However, Li metal anodes are known for poor cycling stability, where large volume change paired with the high reactivity of metallic Li inevitably yields low Coulombic efficiency (CE), limiting the cyclability of practical Li-metal batteries (LMBs)[8–10]. On the other hand, both the capacity retention and operating voltage of LIBs and LMBs are known to suffer severely at temperatures below −30 °C. This performance decrease has been attributed to a number of factors, including increased impedance from bulk ion transport in the electrolyte and migration of Li^+ through the solid–electrolyte interphase (SEI). Most importantly, Li^+ desolvation is believed to be the dominant impedance contributor, and is correlated to the Li^+/solvent binding energy at the interphase[1,11–13]. In general, these resistances have been minimized by employing low-melting-point and/or low-polarizability solvents[1–6,13–21], novel salt additives[21–23] and, most recently, surface functionalization, where Gao et al. demonstrated remarkable Li reversibility down to −115 °C (ref. [24]). Though much progress has been made, methods for directly improving the desolvation kinetics are largely unknown.

This work aims to provide such a method, where the solvation structure of Li^+ in the electrolyte was found to be of great importance to the reversibility and plating behaviour of Li metal at low temperatures. These findings were demonstrated through the systematic comparison of a diethyl ether (DEE), and 1,3-dioxolane/1,2-dimethoxyethane-based (DOL/DME) control electrolyte. After experimental and theoretical investigation of their low-temperature Li plating behaviour, the investigated electrolytes were applied in LMB full-cells with practical electrode loadings, employing a SPAN cathode at a loading of 3.5 mAh cm^{-2} paired with a limited Li anode (N/P capacity ratio = 1). The cells employing the DEE electrolyte retained 76% of their capacity when charged and discharged at −60 °C, compared with only 2.8% in the DOL/DME control system. This study sets a performance standard for the operation of ultra-low-temperature batteries and reveals key electrolyte design strategies at the molecular level to do so.

Low-temperature system design

Low-temperature performance loss of batteries can be mitigated by the addition of warming mechanisms. Recently, progress has been made in limiting the impact to total system mass[25,26]. Battery warming systems, however, consume non-negligible power, which inevitably reduces overall operating efficiency and energy density of low-temperature devices[25,26]. Hence, it is important to consider the operational conditions of low-temperature batteries during system design, which define the requirements of the warming components. In principle, these operation conditions fall under three schemes as shown in Fig. 1, where scheme 3 is required to reduce or eliminate the need for battery warming during continuous operation. Despite this, the low-temperature LIB and LMB communities have primarily focused on low-temperature discharge after charging under mild conditions (scheme 2)[1–6,14,16,18–23]. This focus is likely a result of the kinetic demands of scheme 3, particularly for LMBs due to the challenge of maintaining homogenous Li deposition at ultra-low temperatures, which is a notably difficult proposition even under benign temperatures[8–10].

[1]Department of NanoEngineering, University of California, San Diego, La Jolla, CA, USA. [2]Program of Materials Science, University of California, San Diego, La Jolla, CA, USA. [3]Program of Chemical Engineering, University of California, San Diego, La Jolla, CA, USA. [4]Sustainable Power and Energy Center, University of California, San Diego, La Jolla, CA, USA. ✉e-mail: tpascal@ucsd.edu; zhengchen@eng.ucsd.edu; piliu@eng.ucsd.edu

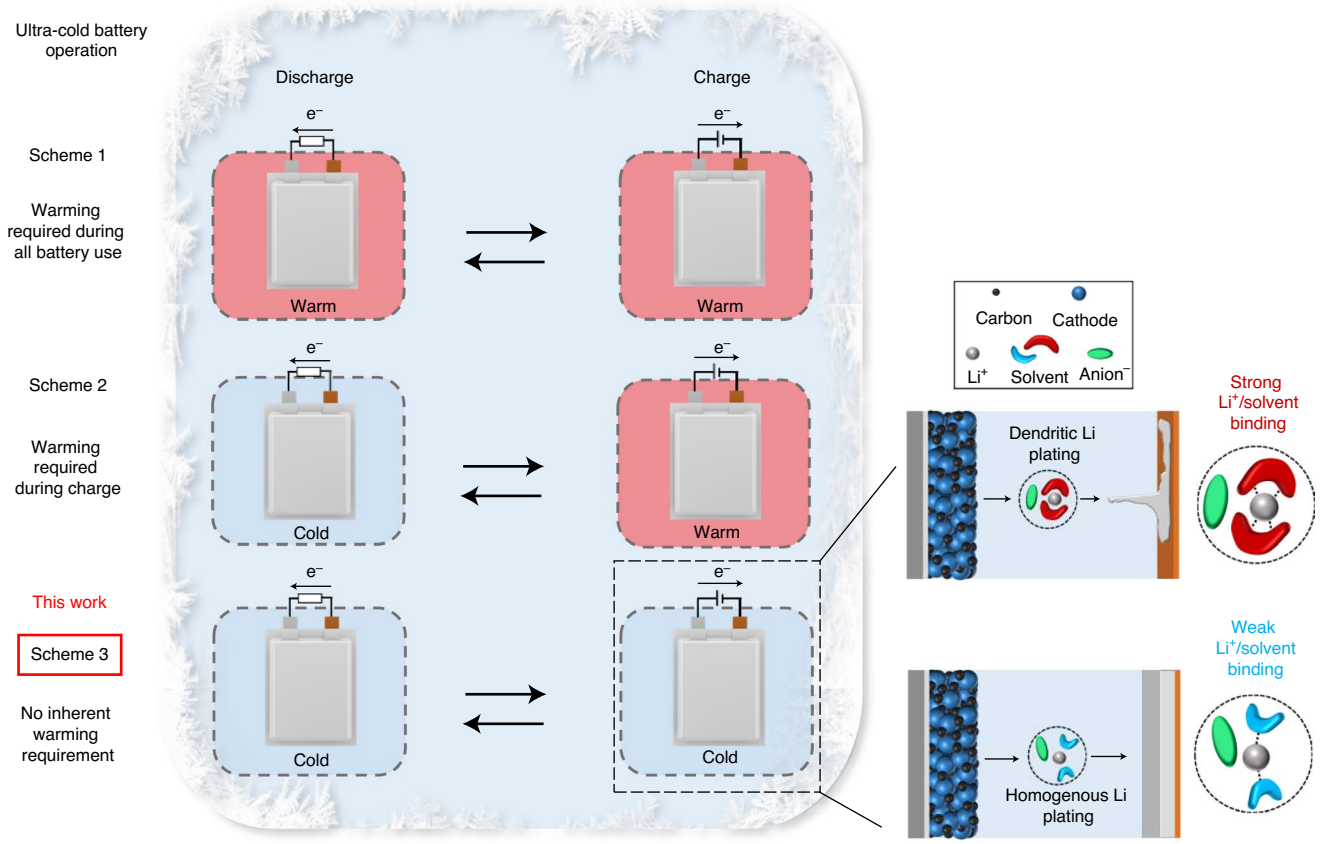

Fig. 1 | Operational schemes of low-temperature LMBs and the significance of their electrolyte structure for ultra-low Li plating. Scheme 1, thermal management required during both charge and discharge processes. Scheme 2, low-temperature discharge capability with thermal management required during charge. Scheme 3, batteries capable of both charge and discharge at low temperature, free of thermal management.

Though reversible LMBs have recently been demonstrated at −15 °C (ref. [24]), there has been very few demonstrations of full-cell LMBs at temperatures below −30 °C (refs. [14–16]), where only Dong et al. have provided low-temperature charge and discharge cycling[15]. This earlier work revealed the significant role of ionic solvation in extending the operational potential window while maintaining ionic conductivity at ultra-low temperature. This work also served to provide an LMB capable of cycling at ultra-low temperature, with a reported CE of 89% at −40 °C. Thus, design strategies for high Li CE at ultra-low temperatures are yet to be established, and the mechanistic understanding of Li plating dynamics at such temperature extremes are largely unknown. These factors had fundamentally limited the deployment of high-energy rechargeable LMBs in extreme environments. In this work, we observe that enabling LMBs at ultra-low temperatures is heavily dependent on optimization of the electrolyte solvation structure, which was found to define the interfacial ion desolvation mechanics and the corresponding Li deposition morphologies (Fig. 1). This evidence was shown by electrolytes based on DEE and DOL/DME solvents, which provided vastly divergent Li metal performance at −40 °C and below, owing to their differing solvation structures, without any correspondence to their SEI composition and ionic conductivity at low temperature.

Ultra-low-temperature Li metal performance

Electrolytes utilizing lithium bis(fluorosulfonyl)imide (LiFSI) are well known to produce some of the highest reported CE values for Li metal anode cycling[27–30]. Hence, 1 M LiFSI was paired with the solvents of interest (Supplementary Table 1) in order to examine their Li metal performance at ultra-low temperature. 1 M LiFSI DOL/DME (1:1 volume) was selected as the control electrolyte due to the large volume of work previously conducted with similar formulations in the field, in addition to the low melting points of both DOL and DME (Supplementary Table 1)[28,31–33]. These electrolytes were first applied to Li||Cu cells, where the Li plating/stripping CE was determined via the method proposed by Adams et al.[34] As shown in Fig. 2a, despite providing an efficiency of 98.9% at room temperature, the CE of the 1 M LiFSI DOL/DME system was found to sharply decrease to 45.4% and 27.5% at −40 °C and −60 °C, respectively. The 1 M LiFSI DEE system, however, was found to maintain CE values of 98.9%, 99.0% and 98.4% at 23 °C, −40 °C and −60 °C, respectively (Fig. 2b). Furthermore, it was found that the DEE system yielded smooth Li deposition/stripping profiles with stable voltage outputs, which was not shared by the DOL/DME system, indicative of soft-shorting events. Additional data demonstrating the superiority of the DEE electrolyte in terms of long term Li||Cu cycling efficiency, critical current density at different temperatures, and faster kinetics at low temperatures as measured by Tafel plots can be found in Supplementary Figs. 1–3.

To confirm the presence of shorting in the DOL/DME system and provide further characterization of the Li metal plated at ultra-low temperatures, high capacity deposition was conducted, where 5 mAh cm^{-2} was deposited at 0.5 mA cm^{-2} in both electrolytes at the temperatures of interest (Fig. 2c,d). The cells were then disassembled to observe the morphology of the plated Li. The photographs taken of the Cu electrodes (Fig. 2e) clearly show that the observable amount of deposited Li in 1 M LiFSI DOL/DME undergoes a severe reduction from 23 °C to −40 °C, where

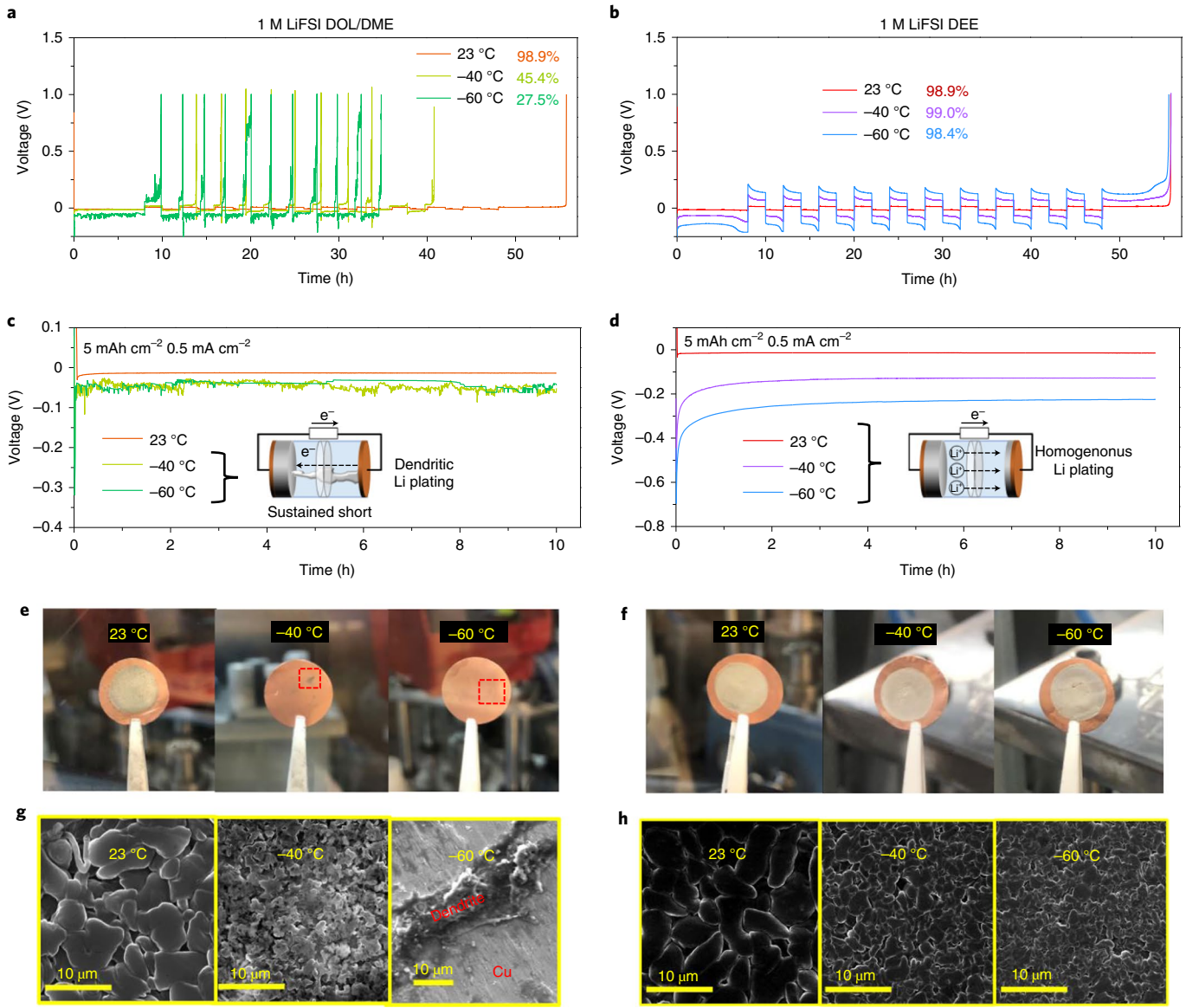

Fig. 2 | Li metal performance and characterization at benign and ultra-low temperatures. a,**b**, Plating/stripping profiles for CE determination in 1 M LiFSI DOL/DME (**a**) and 1 M LiFSI DEE (**b**) at 0.5 mA cm^{-2} with SEI formation steps omitted. **c**,**d**, Li deposition profiles for characterization in 1 M LiFSI DOL/DME (**c**) and 1 M LiFSI DEE (**d**) at 0.5 mA cm^{-2}. **e**,**f**, Optical photographs of Cu current collector after the corresponding deposition experiments in 1 M LiFSI DOL/DME (**e**) and 1 M LiFSI DEE (**f**). The significantly reduced amount of visible Li at −40 and −60 °C in DOL/DME were attributed to shorting. **g**,**h**, SEM images of Li plated in 1 M LiFSI DOL/DME (**g**) and 1 M LiFSI DEE (**h**).

almost no deposits are visible at −60 °C. We believe this is a clear sign of soft shorting, in which the fast growth of dendritic Li serves to form a pathway for electrons in the circuit, rendering further Li^+ migration and conversion unnecessary to balance the charge in the electrochemical circuit. On the other hand, the DEE system yielded visibly uniform silver Li metal depositions down to −60 °C (Fig. 2d). The scanning electron microscopy (SEM) images of the DOL/DME system are shown in Fig. 2g, where the image of plated Li at 23 °C reveals dense Li 'chunks' up to 10 μm in size. The same images were also taken for the sparse Li plated at −40 °C and −60 °C of the red-boxed regions indicated in Fig. 2e, where extremely porous Li was observed at −40 °C, and a single localized dendrite was observed at −60 °C. However, the Li plated at 23 °C, −40 °C and −60 °C in 1 M LiFSI DEE shows the same dense, dendrite-free structure, whose chunk size was found to reduce from ~10 μm to ~1 μm from 23 °C to −60 °C.

Non-correlation between SEI or bulk transport and performance

Though desolvation has been previously attributed to be the dictating step of charge transfer in intercalation-based LIBs, the SEI composition and ionic conductivity was first assessed to determine the presence of any correlations that may relate to the low-temperature performance deviation[12]. Through the application of X-ray photoelectron spectroscopy (XPS), it was found that there was little deviation between the interfacial chemistry of Li cycled 10 times in the DOL/DME and DEE systems, which were largely CO_3, C–O, S–O, Li–O and Li–F, and is in close agreement to Li cycled in other DME/LiFSI-based systems[28]. The chemical similarity of the SEI produced in these two systems corroborates the identical CE at room temperature, and indicates the SEI composition is not likely related to the shorting behaviour found in the DOL/DME based system. (Fig. 3a–c). The SEI composition

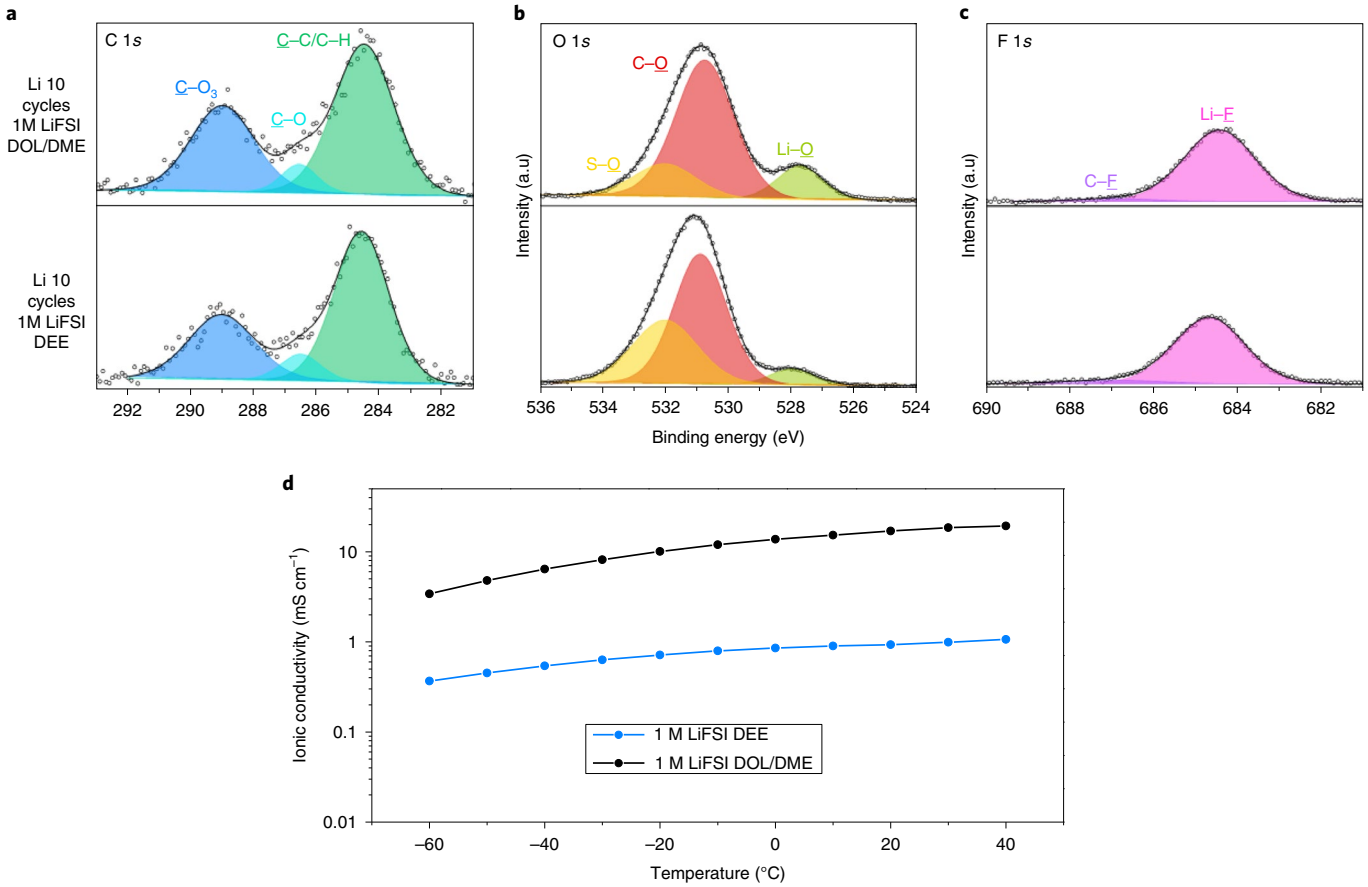

Fig. 3 | Lithium SEI and ionic conductivity study of electrolytes. a–c, Ex-situ XPS of Li anodes after 10 cycles for 1 mAh cm^{-2} at 0.5 mA cm^{-2} in 1 M LiFSI DOL/DME (top) and 1 M LiFSI DEE (bottom) at room temperature. C 1s (**a**), O 1s (**b**) and F 1s (**c**) spectra with assigned peaks from Gaussian/Lorentzian product peak fitting. **d**, Measured ionic conductivity of the investigated electrolytes at different temperatures.

produced by the DEE system at varying temperatures is also provided in Supplementary Fig. 4.

Additionally, the salient deviation of Li metal performance at low temperatures between the DOL/DME and DEE electrolytes cannot be attributed to the reduction of bulk ion transfer in the electrolytes at reduced temperature, where the electrolytes both remain in a liquid state (Supplementary Fig. 5). As shown in Fig. 3d, the measured ionic conductivity of the 1 M LiFSI DOL/DME electrolyte was found to be consistently higher at all measured temperatures, still retaining a remarkable 3.41 mS cm^{-1} at −60 °C, compared with only 0.368 mS cm^{-1} in 1 M LiFSI DEE. It is noteworthy that there was also a deviation in the Li$^+$ transference number between the DOL/DME and DEE systems, which were measured to be 0.314 and 0.512, respectively (Supplementary Fig. 6). While this discrepancy is significant, the tenfold difference in ionic conductivities is expected to overwhelm the difference in transference number in the determination of Li$^+$ transport limitation, as shown in the calculated Sand's capacity for the DEE and DOL/DME electrolytes in Supplementary Fig. 7 using the model proposed by Bai et al.[35]. As maintaining high ionic conductivity at low temperatures has been a historical and intuitively rooted focus of the low-temperature electrolyte field, this case study serves to challenge this trend. Hence, understanding the underlying electrolyte features that yield such salient deviation of Li metal performance in these two systems is vital not only to studying these systems, but to elucidate the molecular design requirements for the future of low-temperature LMBs.

Electrolyte solvation structure and performance impact

Given the non-correspondence of the ionic conductivity and SEI compositions, it is clear that both the improved CE and morphology provided by the DEE system in stark contrast to the catastrophic failure of the DOL/DME system are a result of charge-transfer reactions at the interphase. As previous studies have indicated that Li$^+$ desolvation dominates this process at low temperature, we hypothesize that the desolvation behaviour is a direct result of the inherent solvation structure of the electrolytes, which holds the key to describing the performance discrepancy between the DOL/DME and DEE systems[11,12]. These solvation structures were investigated using both computational and experimental methods.

First, classical molecular dynamics (MD) simulations were conducted with the resulting data shown in Fig. 4a–d. Analysis of the RDF data revealed that 1 M LiFSI in DOL/DME displayed a characteristic solvent-separated ion pair (SSIP) structure, in which the Li$^+$ coordination is dominated by DME molecules, with an average coordination number of 4.6 DME oxygens per Li$^+$. The SSIP structure is well known to persist in similar glyme/Li$^+$ electrolytes, and is characterized by solvation shells dominated by interactions between cation and solvent (Fig. 4e)[35–38]. By contrast, the 1 M LiFSI DEE solution was found to display a characteristic contact-ion pair (CIP) structure, in which the Li$^+$ solvation shell comprises both FSI$^-$ and DEE molecules, with average coordination numbers of 1.8 DEE oxygens and 2.0 FSI$^-$ oxygens per Li$^+$. This CIP structure is well known to exist in electrolytes with a high salt/solvating solvent ratio, and is balanced between both ion/solvent and cation/anion binding (Fig. 4g)[15,27–30,39]. The factors that dictate the formation of SSIP and

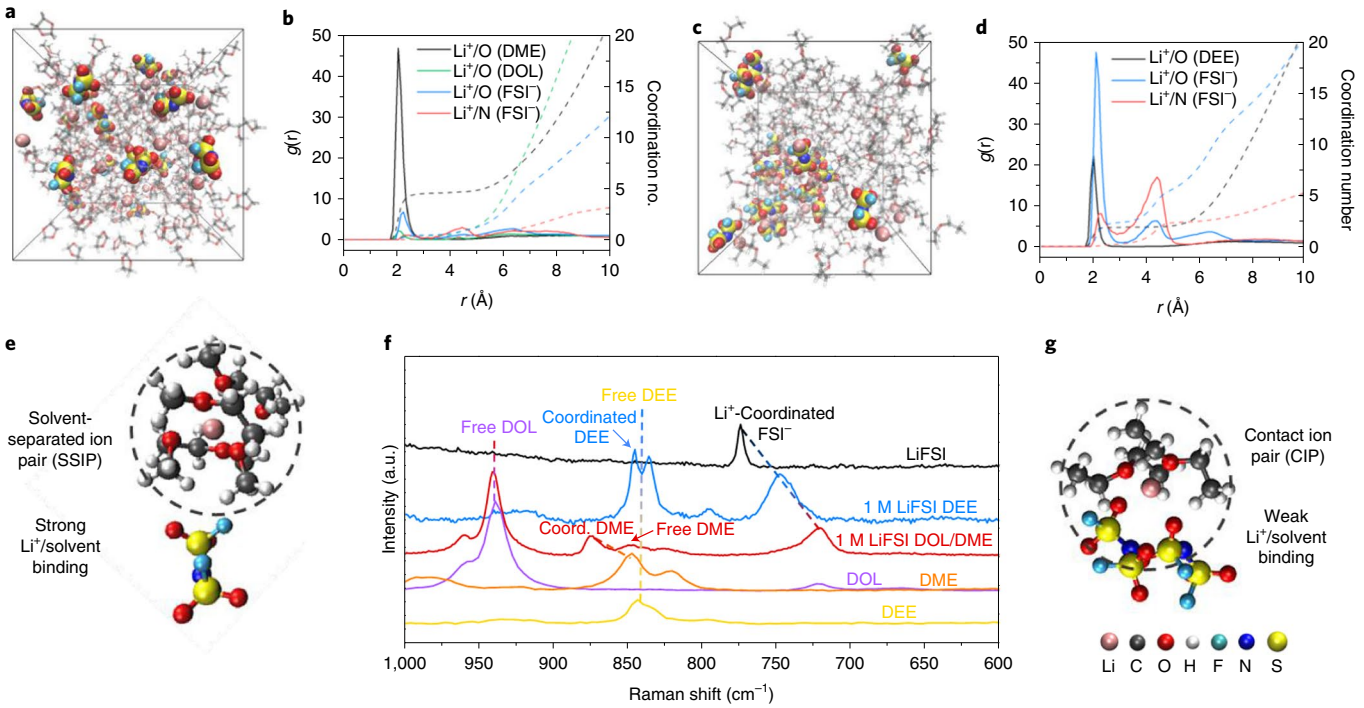

Fig. 4 | Theoretical and experimental analysis of electrolyte structure. a,**b**, Snapshot (**a**) and Li^+ radial distribution function (**b**) obtained from MD simulations of 1 M LiFSI DOL/DME. **c**,**d**, Snapshot (**c**) and Li^+ radial distribution function (**d**) obtained from MD simulations of 1 M LiFSI DEE. **e**, Most probable solvation structure extracted from MD simulation of 1 M LiFSI DOL/DME. **f**, Raman spectra obtained from electrolytes of interest and their components. **g**, Most probable solvation structure extracted from MD simulations of 1 M LiFSI DEE.

CIP structures have yet to be proposed quantitatively, however in thermodynamic terms, solubilities resulting in CIP structures are more entropically driven than the SSIP structures. An expanded discussion of these considerations is provided in Supplementary Note 1.

Experimental evidence of these MD results was obtained from Raman spectra of the electrolytes and their components. These spectra are displayed in Fig. 4f, where the 1 M LiFSI DOL/DME and 1 M LiFSI DEE are compared to the individual LiFSI salt, and the DME, DOL and DEE solvents. It is well known that upon dissolution, the peaks associated with the anion of the Li^+ salt undergoes a significant red shift due to the reduced coordination between cation and anion and increased coordination between cation and solvent[27,40]. As seen in the LiFSI spectra, the S–N–S bending peak of the FSI^- at 774 cm^{-1} undergoes a significant shift to 720 cm^{-1} when dissolved in the DOL/DME solvents, indicating a strong dissociation of the Li^+/FSI^- interactions, in agreement with the MD SSIP solvation structure. Conversely, the FSI^- S–N–S bending peak in 1 M LiFSI DEE undergoes a much smaller shift, from 774 cm^{-1} in the pure salt to only 748 cm^{-1} in the electrolyte, indicative of much stronger Li^+/FSI^- interactions that is characteristic of a CIP structure. The Fourier transform infra-red spectra (FT-IR) for these systems can also be found in Supplementary Fig. 8, where the C–O–C peak of DEE (1,130 cm^{-1}) was found to undergo a reduced shift compared with that of DME (1,106 cm^{-1}) after the introduction of 1 M LiFSI. A further confirmation of the MD accuracy can be found through the calculated transference numbers, which are close to the experimental values for both systems (Supplementary Table 2). Additionally, it is noteworthy that the CIP solvation structure exhibited by the DEE system may be responsible for the improved oxidative stability shown in Supplementary Fig. 9.

The balance between cation/solvent and cation/anion binding in each solvation shell is of particular importance when considering Li^+/Li charge-transfer mechanics at the anode interphase, where these structures can be expected to undergo different dynamics in the presence of an electric field. Specifically, it has been well documented that the significant negative polarization of the anode surface results in the repulsion of anions[9,35,41], and $Li^+/anion^-$ binding has frequently been neglected in the desolvation/solvation energy calculations of previous studies[16,42]. As represented in the proposed mechanisms shown in Fig. 5a,b, the binding energy of the remaining $Li^+(solvent)_n$ complexes were assessed via quantum chemistry simulations, which yielded binding energies of −414 and −280 kJ mol^{-1} for the $Li^+(DME)_{2.3}$ and $Li^+(DEE)_{1.8}$ complexes (average coordination numbers from MD), respectively. It is worthwhile to consider that Li^+ may undergo significant changes in its solvent coordination number at the interface after anion repulsion, however for the purposes of this study it was determined that the binding energy disparity between DME and DEE persists across comparable $Li^+(DME)_n$ and $Li^+(DEE)_n$ complexes for $n = 1$–3 as shown in Supplementary Fig. 10. Hence, the binding energies provided for $Li^+(DME)_{2.3}$ and $Li^+(DEE)_{1.8}$ complexes are meant as a qualitative indication of their divergent desolvation barriers. As the charge-transfer impedance is known to be dominated by Li^+ desolvation at ultra-low temperatures[11,12], we contend that this stark difference in binding energy leads to vastly increased local charge-transfer impedance in the DOL/DME system. Under such severe conditions, it is natural to expect that the Li deposition dynamics would proceed in a tip-driven manner, due to the increased driving force offered by the high-surface-area dendritic Li (Fig. 5a). Such growth would ultimately result in the rampant shorting observed in the 1 M LIFSI DOL/DME system at −40 and −60 °C, whereas the weakly bound DEE system offers homogenous deposition behaviour at these ultra-low temperatures (Fig. 5b).

Further confirmation of the advantages provided by the CIP solvation structure was also observed in additional systems by

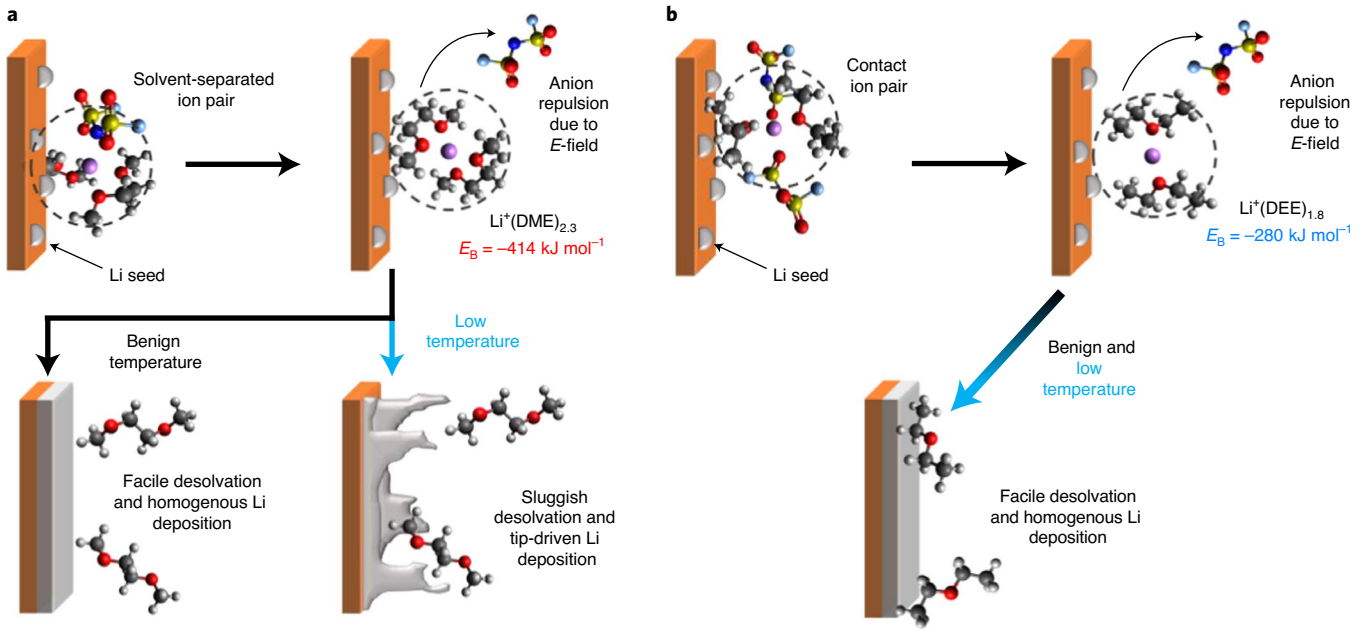

Fig. 5 | Proposed relationship between electrolyte structure and desolvation. a,**b**, Proposed desolvation mechanisms and corresponding Li^+/solvent binding energies obtained from quantum chemistry simulations in 1 M LiFSI DOL/DME (**a**) and 1 M LiFSI DEE (**b**).

changing the salt or the solvent. When the LiFSI salt was replaced by $LiClO_4$ in DOL/DME, evidence of a CIP structure was observed with MD, Raman, ionic conductivity and transference number measurements, and an improvement of low-temperature Li metal shorting behaviour was observed at −20 °C (Supplementary Fig. 12). LiFSI solutions with dipropyl ether (DPE) and dibutyl ether (DBE) are also expected to yield the CIP structure via MD. These electrolytes show similar improvements in performance at −40 °C with CEs of 97.3 and 98.2%, respectively (Supplementary Fig. 13). Additionally, the influence of bulk ion transport and interphasial kinetics on Li metal shorting was examined through the variation of LiFSI concentration in DOL/DME (Supplementary Fig. 14), and DEE (Supplementary Fig. 15). The critical short current of the DEE electrolytes was found to be highly dependent on salt concentration and weakly dependent on temperature due to their superior interphasial kinetics and relatively poor mass transport, while the DOL/DME series were found to display the opposite trend (Supplementary Fig. 16). All of these observations further confirm the advantage of the CIP structure in enabling low-temperature performance for Li metal anodes. A more detailed discussion of these experiments is provided in Supplementary Notes 2–4.

Full-cell behaviour

In order to demonstrate the low-temperature performance of the 1 M LiFSI DEE system, a SPAN cathode was selected as the basis of eventual full-cell construction due to its high capacity, low cost and modest voltage, which satisfies the oxidative stability range of most ether electrolytes[43–45]. The full-cells comprised a SPAN cathode with the high mass loading of 3.5 mAh cm^{-2} paired with a 40 µm Li metal anode, which corresponds to onefold excess capacity (Fig. 6a). Due to the inherent solubility of lithium polysulfides in typical ether solvents, the SPAN cathode is generally discouraged from use[44–47]. However, as displayed in Fig. 6b, DEE does not display the same solubility for polysulfides as the DOL/DME mixture. This reduced dissolution feature is also apparent in the room-temperature voltage profiles found in Supplementary Fig. 17 and the cycling data of the full-cells (Fig. 6c), where the DEE system retained stable cycling performance in contrast to the low initial CE and immediate capacity fade of the DOL/DME system, which can be attributed to polysulfide shuttling[45–47]. Such polysulfide dissolution was also observed via ex-situ FT-IR (Supplementary Fig. 18) and XPS (Supplementary Fig. 19) conducted on delithiated SPAN electrodes after 10 cycles in the electrolytes of interest. In both FT-IR and XPS, clear Li–S signals were observed on the electrodes cycled in the DOL/DME system, which is attributed to residual polysulfides and is not found in the DEE cycled electrodes. It is also noteworthy that the formation of polysulfides in the DOL/DME electrolyte during cycling may also interfere with the production of a stable cathode–electrolyte interphase (CEI), as both C 1*s* signals and Li–F peaks were found to be diminished in the DOL/DME cycled electrode, whereas clear peaks were still visible in the DEE cycled electrodes, particularly for Li–F.

A similar cycling trend was also observed in half cells, where the DEE system retained stable performance at both 0.5 mAh cm^{-2} and 3.5 mAh cm^{-2} cathode loadings, while the DOL/DME system's poor cycling stability and low CE is clearly evident at 0.5 mAh cm^{-2} loading and significantly exacerbated at 3.5 mAh cm^{-2} (Supplementary Fig. 20). These cells were then subjected to cycling at −40 °C and −60 °C to satisfy the design requirements of operating scheme 3 as previously discussed. The voltage profiles for the DEE and DOL/DME full-cells cycled at −40 °C and −60 °C and a 0.1 C rate are shown in Fig. 6d,f, where it was found that the 1 M LiFSI DOL/DME electrolyte produced diminished output capacities of 236 mAh g^{-1} and 13 mAh g^{-1}, which correspond to 38.9% and 2.8% of the capacity produced at room temperature, respectively. On the other hand, the 1 M LIFSI DEE system was found to produce improved capacities of 519 mAh g^{-1} and 474 mAh g^{-1} at the same conditions, which corresponds to room-temperature capacity retentions of 84% and 76%, respectively. The variance in cell performance was found to be primarily attributable to charge transfer at low temperature, which is shown via electrochemical impedance spectroscopy (EIS) in Supplementary Fig. 21.

The full-cells based on these two electrolytes were then cycled at −40 °C and −60 °C in order to provide the wholistic effect of both the Li metal anode and SPAN cathode performance at ultra-low temperatures. As shown in Fig. 6e, the 1× Li||SPAN full-cell utilizing 1 M LiFSI DOL/DME at −40 °C was found to undergo severe

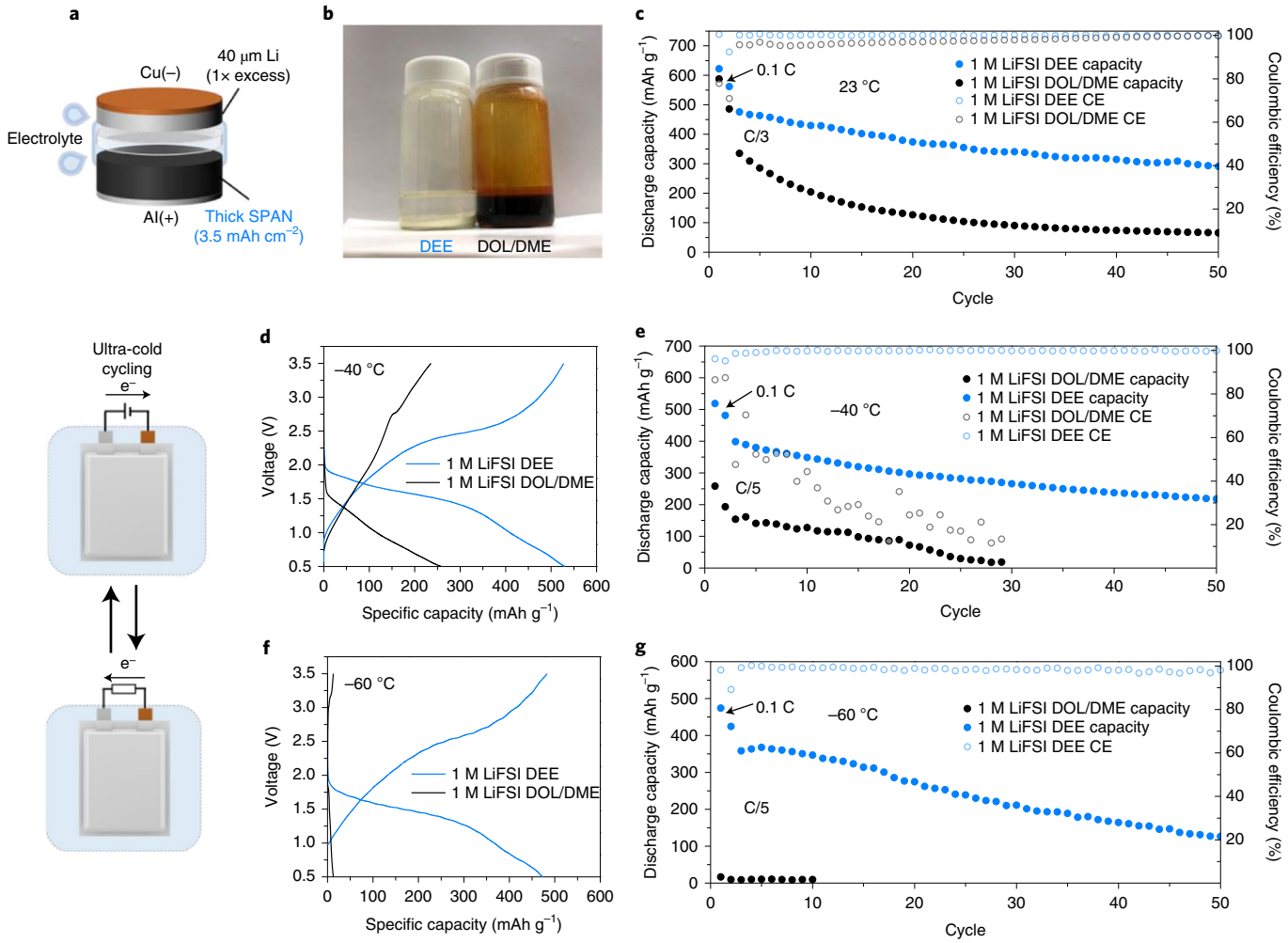

Fig. 6 | 1× Li||SPAN full-cell performance at benign and ultra-low temperature. a, Schematic of the demonstrated full cells. **b**, Dissolution photograph of 0.25 M Li_2S_6 obtained by stirring stoichiometric amounts of Li_2S and S for 24 h. **c**, Cycling performance of full cells in each electrolyte at 23 °C and 0.333 C rate. **d**,**e**, 0.1 C charge/discharge profiles (**d**) and cycling performance (**e**) at −40 °C and 0.2 C. **f**,**g**, 0.1 C charge/discharge profiles (**f**) and cycling performance (**g**) at −60 °C and 0.2 C.

capacity fade after only two cycles of operation, where the low CE observed starting on the third cycle was taken to be clear evidence of the exhaustion of the onefold excess Li reserve. Furthermore, the same full cell utilizing 1 M LiFSI DOL/DME was found to provide no viable capacity output after 2 cycles at −60 °C (Fig. 6g). On the other hand, the 1× Li||SPAN full-cell was able to provide reliable cycling performance at both −40 °C and −60 °C (Fig. 6e,g).

Comparison with the state of the art

To put this work in a historical perspective, we calculated the energy density of previously published systems based on the 18,650 cell-level projection model proposed by Betz et al.[48] with the details outlined in the experimental section. The fundamental appeal of LMBs is their ability to achieve higher energy densities than those of LIBs, however until very recently there had not been a practical demonstration of a rechargeable LMB exceeding the theoretical limit of a LIB 18,650 cylinder cell (~250 Wh kg^{-1}) at the cell level projected using the above model[29]. Intuitively, state-of-the-art low-temperature LMBs are behind ambient temperature LMBs due to the inherently more difficult considerations of system design. For this reason, all of the cell demonstrations to date have employed Li metal anodes of excess capacity, often paired with cathodes of low mass loading[14–16]. Moreover, no LIB or LMB has ever demonstrated both charge and discharge at ultra-low temperatures with the notable exceptions of Cho et al.[49] and Dong et al.[15] It is also worth noting that while our previous work has demonstrated an LMB system with practical Li loading capable of ultra-low temperature discharge, the correspondingly high energy densities of this system are not expected to be sustained if the charging was carried out at low temperatures, particularly given the cell shorting considerations outlined above[50].

In this regard, this work is a significant step both in diagnosing the challenge of plating Li at ultra-low temperatures and high CE, as well as providing the criteria required to overcome this challenge via solvation chemistry of the electrolyte. In doing so we have provided a route to practical LMB full-cells with cell-level energy densities of 218, 143 and 126 Wh kg^{-1} when charged and discharged at 23, −40 and −60 °C (Fig. 7a), respectively. This performance compares favourably with other LMB and LIB energy densities at the same temperatures, the majority of which were charged at room temperature before low-temperature discharge. A quantitative comparison of the practical considerations of low-temperature LMBs can be found in Fig. 7b corresponding to the metrics listed in Supplementary Table 3.

It is worth noting that depending on the application for a given system, safety should also be considered. To provide a first step in

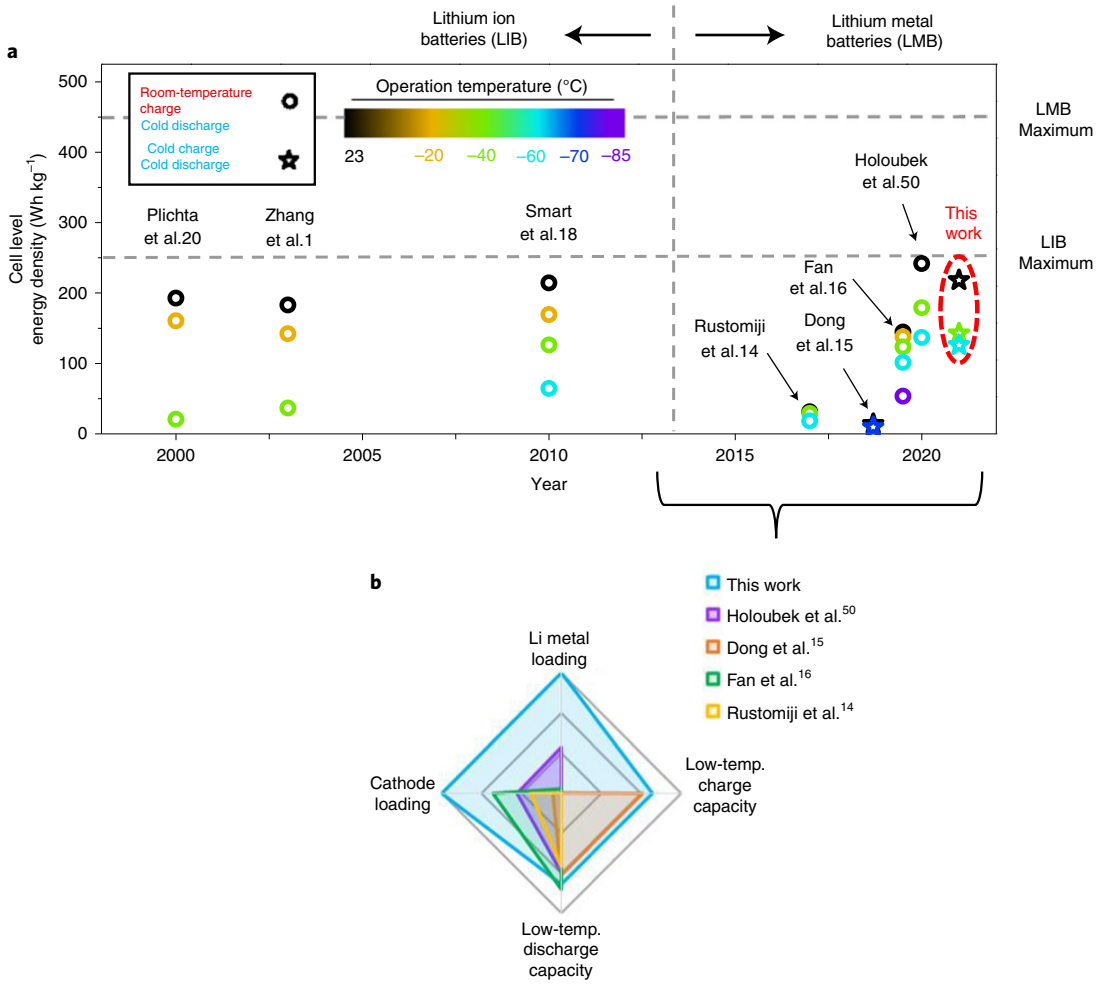

Fig. 7 | The historical context of this work. a, Cell-level energy density of selected low-temperature batteries by publication year. Energy densities were calculated based on the 18,650 cylinder cell model proposed by Betz et al.[48] using the assumptions outlined in the experimental details. **b**, Comparison of relevant low-temperature LMBs as quantified by Supplementary Table 3, where loading values are normalized to the highest reported values in literature and the capacity retention values are normalized to 100%. It is noteworthy that the ostensibly greater energy densities from previous works are not expected to be upheld under low-temperature charging.

demonstrating the scalability and potential safety risks associated with LMBs at ultra-low temperature, we have assembled a 160 mAh Li||SPAN pouch cell utilizing a further increased cathode loading of 6 mAh cm^{-2} (Supplementary Fig. 23a). This pouch cell was able to produce a capacity of 450 mAh g^{-1} when charged and discharged at −40 °C, which compares favourably to the coin-cell performance given the increased loading and overall cell size (Supplementary Fig. 23b). Furthermore, when put under soft-shorting conditions at −40 °C, the cell temperature was found to change negligibly, indicating that this process may not result in catastrophic outcomes at such operating temperatures (Supplementary Fig. 23c).

Conclusions

In summary, we have demonstrated that electrolyte solvation structure is crucial to enable the reversible cycling of Li metal at ultra-low temperatures primarily through the comparative study of 1 M LiFSI DEE and 1 M LiFSI DOL/DME. These insights, as well as the performance metrics provided by the 1 M LiFSI DEE system were leveraged to produce a full-cell with practical electrode loadings that promise to enable LMBs cycled at 23 °C, −40 °C and −60 °C. This work represents a significant advancement in the design of low-temperature batteries, both in concept and demonstration, and sets a new performance standard that promises to yield systems that exceed previous energy density limitations while reducing or eliminating the need for battery warming systems due to their universal operating capabilities at ultra-low temperatures.

Methods

Materials. The electrolyte materials DOL and DME were purchased from Gotion and used as received. DEE was purchased from Sigma-Aldrich, and LiFSI was obtained from Capchem. The electrolytes were prepared by dissolving predetermined amounts of LiFSI salt into the solvents of interest and stirred.

The SPAN electrodes were prepared by hand milling polyacrylonitrile (Sigma-Aldrich, M_w = 150,000) and elemental sulfur (Sigma-Aldrich) in a mortar with a mass ratio of 1:4 until a homogenous mixture was obtained. The mixed powders were heated in an argon-filled tube furnace at 450 °C for 6 hours with a ramp rate of 2 °C min^{-1}, then cooled down to room temperature. The SPAN cathode was prepared by mixing the synthesized SPAN powder, Super-P and PVDF (KYNAR 2800) in a ratio of 80:10:10 in *N*-methyl pyrrolidinone solvent, cast on carbon-coated Al foil and dried overnight in a vacuum oven at 60 °C.

For electrochemical tests CR-2032-type coin cells were assembled with prepared cathodes and anodes separated by a 25 µm Celgard membrane soaked with 75 µl of electrolyte. It is noteworthy that the cells were first assembled dry and electrolyte injection was saved for the last step before crimping in order to minimize evaporation of the DEE solvent. For Li metal performance tests, 250 µm Li metal chips were purchased from Xiamen TOB New Energy Technology and paired with Cu foil for Li||Cu cells, or an identical Li chip in Li||Li cells. The Li||SPAN half cells were assembled with a 250 µm chip and the prepared SPAN cathodes. Linear scan voltammetry (LSV) stability tests were conducted with 250 µm Li and a blocking working electrode made of Al foil. 1× Li||SPAN full-cells

were assembled with a 3.5 mAh cm^{-2} SPAN electrode and a thin Li electrode obtained from China Energy Lithium, which was determined via SEM to be 40 µm thick. Two Celgard separators were employed in the full-cells in an attempt to mitigate shorting during cycling.

Characterization. The morphology of the deposited Li metal at various temperatures was characterized using an FEI Quanta 250 SEM. The samples were obtained from coin cells and washed with either DEE or DME before analysis. XPS (Kratos Analytical, Kratos AXIS Supra) was carried out using an Al anode source at 15 kV and all the peaks were fitted based on the reference C–C bond at 284.6 eV on both Li metal and SPAN samples. All XPS measurements were collected with a 300 mm × 700 mm spot size during acquisition. Survey scans were collected with a 1.0 eV step size, and were followed by high-resolution scans with a step size of 0.05 eV for C 1*s*, O 1*s*, F 1*s* and S 2*p* regions. All prepared samples were placed in a heat-sealed bag inside the glovebox before they were transferred to the XPS and SEM. SPAN electrodes before and after 10 cycles in 1 M LiFSI DEE and DOL/DME were analysed by a Perkin Elmer FT-IR. The polysulfide dissolution tests were performed by immersing stoichiometric ratios of Li_2S and S corresponding to 0.25 M Li_2S_6 in DEE and DOL/DME (1:1) solvents and stirring for 24 h.

The ionic conductivity of the electrolyte was measured by a customized two-electrode cell, in which the two polished 316 stainless-steel electrodes were spaced symmetrically at a set distance. The cell constant is frequently calibrated by using OAKTON 0.447 to 80 mS cm^{-1} standard conductivity solution. The electrolytic conductivity value was obtained with a floating AC signal at a frequency determined by the phase angle minima given by EIS using the following equation:

$$\sigma = \frac{L}{A \times R} \tag{1}$$

where R is the resistance, and A and L are the area of and space between the electrodes, respectively. The data points from 40 °C to −60 °C were measured by LabView Software, which was also used to control an ESPEC BTX-475 temperature chamber to maintain the cell at a set temperature for 30-minute intervals during measurement.

Sand's capacity projections were calculated using the following equation[35]:

$$C_{\text{Sand}} = \pi\left(\frac{m_{\text{Li}^+} D_{\text{FSI}^-} + m_{\text{FSI}^-} D_{\text{Li}^+}}{m_{\text{Li}^+} + m_{\text{FSI}^-}}\right)\left(\frac{C^*_{\text{Li}^+} e}{2j} * \frac{1}{(1 - t_{\text{Li}^+})}\right) \tag{2}$$

Where m is the mobility and D is the diffusion coefficient of ionic species, $C^*_{\text{Li}^+}$ is the bulk Li^+ concentration, j is the areal current density, e is the elementary charge and t_{Li^+} is the Li^+ transference number.

Electrochemical testing. All electrochemical data provided in this work were produced by CR-2032-type coin cells or heat-sealed pouch cells assembled in an Ar-filled glovebox kept at <0.5 ppm O_2 and <0.1 ppm H_2O. All low-temperature data points were obtained from these cells inside SolidCold C4-76A and SolidCold C-186A ultra-low chest freezers for −40 °C and −60 °C tests, respectively. All galvanostatic testing was done on an Arbin LBT-10V5A system and all potentiostatic tests were carried out on a Biologic VSP-300 potentiostat.

For Li metal CE determinations, the accurate CE test popularized by Adams et al.[34] was carried out on Li||Cu cells. Prior to the test, a condition cycle was carried out on all the cells, where 4 mAh cm^{-2} of Li was deposited onto the Cu foil at 0.5 mA cm^{-2}, and then fully stripped to 1 V to form the SEI before CE testing. During testing 4 mAh cm^{-2} was first deposited followed by 10 cycles of 1 mAh cm^{-2} plating and stripping before finally stripping all Li to 1 V. The CE was calculated by dividing the total stripped capacity by the total plated capacity. The morphological Li studies at various temperatures were conducted on Cu working electrodes plated with 5 mAh cm^{-2} at 0.5 mA cm^{-2} at room temperature as well as −40 °C and −60 °C after resting for 2 hours to achieve temperature equilibration.

EIS tests of Li||Li cells were carried out on a Biologic VSP-300 potentiostat with a 10 mV perturbation in the frequency range of 1 MHz to 100 mHz. In the case of biased EIS tests, 100 mV was applied to the cell for 2 hours before taking the impedance spectra, and the same bias was applied during the EIS measurement.

The transference numbers of the electrolytes were determined via a commonly applied potentiostatic polarization technique on a Biologic VSP-300 potentiostat in which 5 mV was applied for 2 h to a Li||Li cell with five Celgard separators to obtain the initial current I_0, where the cation concentration is uniform and the current corresponds to both the cations and anions, and the steady state current I_{ss}, which is only attributed to the cations. EIS was applied before and after the polarization on a in order to obtain the cell impedance, where the transference number was then calculated using the following equation:

$$t_+ = \frac{I_{SS}(\Delta V - I_0 R_0)}{I_0(\Delta V - I_{SS} R_{SS})} \tag{3}$$

where ΔV is the applied bias, R_0 is the initial cell impedance and R_{SS} is the steady state cell impedance. The oxidative stability of the electrolytes was determined via LSV of a Li||Al cell at 1 mV s^{-1}.

Li||SPAN cells were assembled and subjected to galvanostatic cycling at room temperature and −40 °C and −60 °C inside the respective chest freezers after resting for 2 h to achieve temperature equilibration. Li||SPAN half cells utilized of 250 µm Li counter electrodes with either 0.5 mAh cm^{-2} or 3.5 mAh cm^{-2} SPAN electrodes. Li||SPAN full cells consisted of 40 µm Li anodes paired with 3.5 mAh cm^{-2} SPAN cathodes, which corresponds to a onefold Li anode excess (N/P = 1) for the SPAN after lithiation.

Three-electrode pouch cells consisted of a 12 mm diameter SPAN or 15 mm diameter Li working electrode, a 15 mm diameter Li counter electrode and a Li reference electrode slightly outside the ionic path of the two electrodes sandwiched between two Celgard separators. Tabs were sealed to the pouch bag using an MTI MSK-140 compact heating sealer. The selected electrodes were attached to the tabs in the Ar-filled glovebox and were sealed using a table-top impulse heat sealer after electrolyte injection. The Li||Li||Li pouch cells were subjected to LSV measurements at room temperature and −40 °C at 1 mV s^{-1} down to −100 mV versus Li. The SPAN||Li||Li pouch cells were subjected to EIS measurements (same conditions as above) at room temperature and −40 °C directly after discharging them to 50% SOC at the selected temperature to avoid encountering nucleation impedance on the anode side. The two-electrode SPAN||Li pouch cell was prepared using a 6 mAh cm^{-2} SPAN cathode cut to 4.4 × 5.7 cm using an MTI MSK-180 punch and a copper anode to which Li was rolled onto inside the glovebox. The sealing procedure matched the three-electrode pouch cells. The two-electrode pouch was subject to ~100 kPa of pressure using two parallel plates fastened together by screws. Temperature monitoring for the two-electrode pouch was conducted with a HOBO thermocouple attached directly to the outside of the pouch on the cathode side and recorded using the HOBO data logger software.

MD simulations. MD simulations were performed in LAMMPS using the OPLS-AA forcefield[51] with the FSI molecules description from Gaouveia et al.[52] For electrolyte structure determination, simulation boxes containing 20 LiFSI molecules and 192 DEE, or 96 DME + 143 DOL molecules corresponding to 1 M LiFSI DEE and 1 M LiFSI DOL/DME (1:1 volume) electrolytes, respectively. Similarly, 1 M $LiClO_4$ DOL/DME and 1 M LiFSI DPE simulations were carried out in boxes composed of 20 salt molecules and 96 DME + 143 DOL, and 147 DPE molecules. In all cases, the charges of the Li^+ and FSI^- molecules were scaled to the high-frequency dielectric properties of the solvents present in the system according to the method proposed by Park et al.[36] For each system, an initial energy minimization at 0 K (energy and force tolerances of 10^{-4}) was performed to obtain the ground-state structure. After this, the system was slowly heated from 0 K to room temperature at constant volume over 0.2 ns using a Langevin thermostat, with a damping parameter of 100 ps. The system was then subjected to five cycles of quench-annealing dynamics, where the temperature was slowly cycled between 298 K and 894 K over 0.8 ns in order to eliminate the persistence of any meta-stable states. After annealing, the system was equilibrated in the constant temperature (298 K), constant pressure (1 bar) (NpT ensemble) for 0.5 ns before finally being subjected to 5 ns of constant volume, constant temperature dynamics. Radial distribution functions were obtained using the Visual Molecular Dynamics (VMD) software. Snapshots of the most probable solvation shells were also sampled from the simulation trajectory using VMD. Transference numbers were calculated from the MD trajectories through a mean-squared displacement analysis over the duration of the constant volume dynamics.

Quantum chemistry calculations. Quantum chemistry simulations were performed using the Q-Chem 5.1 quantum chemistry package at the PBE/6–31 G+(d,p) level of theory, which has previously been shown to produce accurate binding energies[42]. Binding energies of the $Li^+(Solvent)_x$ complexes were calculated after geometry optimizations, where the full complexes were optimized with and without Li^+, representing their separation at infinite distance. The binding energy was calculated as: $E_B = E_{\text{Li}^+(\text{solvent})_x} - \left(E_{\text{Li}^+} + E_{x(\text{solvent})}\right)$. The fractional $Li^+(DME)_{2.3}$ and $Li^+(DEE)_{1.8}$ binding energies were calculated via linear interpolation of the $Li^+(DME)_3$, $Li^+(DME)_2$ and $Li^+(DEE)_1$, $Li^+(DEE)_2$ complex binding energies, respectively.

Cell-level energy density calculations. The cell-level energy densities for this and previous works were calculated via the 18,650 cylinder cell model proposed by Betz et al.[48] previously. As the previous LIB works were generally conducted using commercially produced cells, it was assumed that the cathode loading was 2.5 mAh cm^{-2} given the lower loadings generally applied from 2000–2010 with an N/P cathode/anode capacity ratio of 1.1. For metal-oxide-based cathodes, the active loading was assumed to be 96%, while polymer-based electrodes were assumed to be 90%. The volume change during discharge was determined to be 20% for LIB chemistries and −20% for the Li||SPAN full-cell, which are conservative estimates compared with the previous work, and align with the differences between LIBs and LMBs[48]. The macroscopic volume change of the previous LMBs were assumed to be 0% given the excess anode capacities of the previous LMB works. For all works, it was assumed that a 30% electrode porosity and an electrolyte loading of 2 g Ah^{-1} was achievable and were used in the calculation. For the LMB works, the electrode loadings provided in the original publications were used.

Data availability

All relevant data are included in the paper and its Supplementary Information.

Received: 16 April 2020; Accepted: 21 January 2021;
Published online: 25 February 2021

References

1. Zhang, S. S., Xu, K. & Jow, T. R. The low temperature performance of Li-ion batteries. *J. Power Sources* **115**, 137–140 (2003).
2. Smart, M. C. et al. The use of lithium-ion batteries for JPL's Mars missions. *Electrochim. Acta* **268**, 27–40 (2018).
3. Gupta, A. & Manthiram, A. Designing advanced lithium-based batteries for low-temperature conditions. *Adv. Energy Mater.* **10**, 2001972 (2020).
4. Huang, C.-K., Sakamoto, J. S., Wolfenstine, J. & Surampudi, S. The limits of low-temperature performance of Li-ion cells. *J. Electrochem. Soc.* **147**, 2893–2896 (2000).
5. Plichta, E. J. et al. Development of low temperature Li-ion electrolytes for NASA and DoD applications. *J. Power Sources* **94**, 160–162 (2001).
6. Li, Q. et al. Wide-temperature electrolytes for lithium-ion batteries. *ACS Appl. Mater. Interfaces* **9**, 18826–18835 (2017).
7. Liu, J. et al. Pathways for practical high-energy long-cycling lithium metal batteries. *Nat. Energy* **4**, 180–186 (2019).
8. Xu, W. et al. Lithium metal anodes for rechargeable batteries. *Energy Environ. Sci.* **7**, 513–537 (2014).
9. Li, S. et al. Developing high-performance lithium metal anode in liquid electrolytes: challenges and progress. *Adv. Mater.* **30**, 1706375 (2018).
10. Zhou, H., Yu, S., Liu, H. & Liu, P. Protective coatings for lithium metal anodes: recent progress and future perspectives. *J. Power Sources* **450**, 227632 (2020).
11. Xu, K., von Cresce, A. & Lee, U. Differentiating contributions to "ion transfer" barrier from interphasial resistance and Li^+ desolvation at electrolyte/graphite interface. *Langmuir* **26**, 11538–11543 (2010).
12. Li, Q. et al. Li^+-desolvation dictating lithium-ion battery's low-temperature performances. *ACS Appl. Mater. Interfaces* **9**, 42761–42768 (2017).
13. Holoubek, J. et al. Exploiting mechanistic solvation kinetics for dual-graphite batteries with high power output at extremely low temperature. *Angew. Chem. Int. Ed.* **58**, 18892–18897 (2019).
14. Rustomji, C. S. et al. Liquefied gas electrolytes for electrochemical energy storage devices. *Science* **356**, eaal4263 (2017).
15. Dong, X. et al. High-energy rechargeable metallic lithium battery at −70 °C enabled by a cosolvent electrolyte. *Angew. Chem. Int. Ed.* **58**, 5623–5627 (2019).
16. Fan, X. et al. All-temperature batteries enabled by fluorinated electrolytes with non-polar solvents. *Nat. Energy* **4**, 882–890 (2019).
17. Dong, X., Guo, Z., Guo, Z., Wang, Y. & Xia, Y. Organic batteries operated at −70 °C. *Joule* **2**, 902–913 (2018).
18. Smart, M. C., Ratnakumar, B. V., Chin, K. B. & Whitcanack, L. D. Lithium-ion electrolytes containing ester cosolvents for improved low temperature performance. *J. Electrochem. Soc.* **157**, A1361–A1374 (2010).
19. Smart, M. C. et al. Gel polymer electrolyte lithium-ion cells with improved low temperature performance. *J. Power Sources* **165**, 535–543 (2007).
20. Plichta, E. J. & Behl, W. K. A low-temperature electrolyte for lithium and lithium-ion batteries. *J. Power Sources* **88**, 192–196 (2000).
21. Smart, M. C., Lucht, B. L., Dalavi, S., Krause, F. C. & Ratnakumar, B. V. The effect of additives upon the performance of MCMB/$LiNi_xCo_{1-x}O_2$ Li-ion cells containing methyl butyrate-based wide operating temperature range electrolytes. *J. Electrochem. Soc.* **159**, A739–A751 (2012).
22. Zhang, S. S., Xu, K. & Jow, T. R. A new approach toward improved low temperature performance of Li-ion battery. *Electrochem. Commun.* **4**, 928–932 (2002).
23. Liao, B. et al. Designing low impedance interface films simultaneously on anode and cathode for high energy batteries. *Adv. Energy Mater.* **8**, 1800802 (2018).
24. Gao, Y. et al. Low-temperature and high-rate-charging lithium metal batteries enabled by an electrochemically active monolayer-regulated interface. *Nat. Energy* **5**, 534–542 (2020).
25. Wang, C.-Y. et al. Lithium-ion battery structure that self-heats at low temperatures. *Nature* **529**, 515–518 (2016).
26. Ji, Y. & Wang, C. Y. Heating strategies for Li-ion batteries operated from subzero temperatures. *Electrochim. Acta* **107**, 664–674 (2013).
27. Chen, S. et al. High-voltage lithium-metal batteries enabled by localized high-concentration electrolytes. *Adv. Mater.* **30**, 1706102 (2018).
28. Qian, J. et al. High rate and stable cycling of lithium metal anode. *Nat. Commun.* **6**, 6362 (2015).
29. Niu, C. et al. High-energy lithium metal pouch cells with limited anode swelling and long stable cycles. *Nat. Energy* **4**, 551–559 (2019).
30. Ren, X. et al. Enabling high-voltage lithium-metal batteries under practical conditions. *Joule* **3**, 1662–1676 (2019).
31. Zhang, X.-Q. et al. Regulating anions in the solvation sheath of lithium ions for stable lithium metal batteries. *ACS Energy Lett.* **4**, 411–416 (2019).
32. Thenuwara, A. C., Shetty, P. P. & McDowell, M. T. Distinct nanoscale interphases and morphology of lithium metal electrodes operating at low temperatures. *Nano Lett.* **19**, 8664–8672 (2019).
33. Wang, J. et al. Improving cyclability of Li metal batteries at elevated temperatures and its origin revealed by cryo-electron microscopy. *Nat. Energy* **4**, 664–670 (2019).
34. Adams, B. D., Zheng, J., Ren, X., Xu, W. & Zhang, J.-G. Accurate determination of Coulombic efficiency for lithium metal anodes and lithium metal batteries. *Adv. Energy Mater.* **8**, 1702097 (2018).
35. Bai, P., Li, J., R. Brushett, F. & Bazant, Z. M. Transition of lithium growth mechanisms in liquid electrolytes. *Energy Environ. Sci.* **9**, 3221–3229 (2016).
36. Park, C. et al. Molecular simulations of electrolyte structure and dynamics in lithium–sulfur battery solvents. *J. Power Sources* **373**, 70–78 (2018).
37. Callsen, M., Sodeyama, K., Futera, Z., Tateyama, Y. & Hamada, I. The solvation structure of lithium ions in an ether based electrolyte solution from first-principles molecular dynamics. *J. Phys. Chem. B* **121**, 180–188 (2017).
38. Chaban, V. Solvation of lithium ion in dimethoxyethane and propylene carbonate. *Chem. Phys. Lett.* **631–632**, 1–5 (2015).
39. Ueno, K. et al. Glyme–lithium salt equimolar molten mixtures: concentrated solutions or solvate ionic liquids? *J. Phys. Chem. B* **116**, 11323–11331 (2012).
40. Suo, L., Zheng, F., Hu, Y.-S. & Chen, L. FT-Raman spectroscopy study of solvent-in-salt electrolytes. *Chin. Phys. B* **25**, 016101 (2016).
41. Sand, H. J. S. III On the concentration at the electrodes in a solution, with special reference to the liberation of hydrogen by electrolysis of a mixture of copper sulphate and sulphuric acid. *Philos. Mag.* **1**, 45–79 (1901).
42. Borodin, O. et al. Competitive lithium solvation of linear and cyclic carbonates from quantum chemistry. *Phys. Chem. Chem. Phys.* **18**, 164–175 (2016).
43. Wei, S., Ma, L., Hendrickson, K. E., Tu, Z. & Archer, L. A. Metal–sulfur battery cathodes based on PAN–sulfur composites. *J. Am. Chem. Soc.* **137**, 12143–12152 (2015).
44. Yang, H., Chen, J., Yang, J. & Wang, J. Prospect of sulfurized pyrolyzed poly(acrylonitrile) (S@pPAN) cathode materials for rechargeable lithium batteries. *Angew. Chem. Int. Ed.* **59**, 7306–7318 (2019).
45. Xing, X. et al. Cathode electrolyte interface enabling stable Li–S batteries. *Energy Storage Mater.* **21**, 474–480 (2019).
46. Chen, X. et al. Ether-compatible sulfurized polyacrylonitrile cathode with excellent performance enabled by fast kinetics via selenium doping. *Nat. Commun.* **10**, 1021 (2019).
47. Zhou, J. et al. A new ether-based electrolyte for lithium sulfur batteries using a S@pPAN cathode. *Chem. Commun.* **54**, 5478–5481 (2018).
48. Betz, J. et al. Theoretical versus practical energy: a plea for more transparency in the energy calculation of different rechargeable battery systems. *Adv. Energy Mater.* **9**, 1803170 (2019).
49. Cho, Y.-G., Kim, Y.-S., Sung, D.-G., Seo, M.-S. & Song, H.-K. Nitrile-assistant eutectic electrolytes for cryogenic operation of lithium ion batteries at fast charges and discharges. *Energy Environ. Sci.* **7**, 1737–1743 (2014).
50. Holoubek, J. et al. An all-fluorinated ester electrolyte for stable high-voltage Li metal batteries capable of ultra-low-temperature operation. *ACS Energy Lett.* **5**, 1438–1447 (2020).
51. Kaminski, G. A., Friesner, R. A., Tirado-Rives, J. & Jorgensen, W. L. Evaluation and reparametrization of the OPLS-AA force field for proteins via comparison with accurate quantum chemical calculations on peptides. *J. Phys. Chem. B* **105**, 6474–6487 (2001).
52. Gouveia, A. S. L. et al. Ionic liquids with anions based on fluorosulfonyl derivatives: from asymmetrical substitutions to a consistent force field model. *Phys. Chem. Chem. Phys.* **19**, 29617–29624 (2017).
53. Towns, J. et al. XSEDE: accelerating scientific discovery. *Comput. Sci. Eng.* **16**, 62–74 (2014).

Acknowledgements

This work was supported by a NASA Space Technology Graduate Research Opportunity. This work was also partially supported by the Office of Vehicle Technologies of the US Department of Energy through the Advanced Battery Materials Research (BMR) Program (Battery500 Consortium) under contract no. DE-EE0007764 to P.L. This work was also partially supported by an Early Career Faculty grant from NASA's Space Technology Research Grants Program (ECF 80NSSC18K1512) to Z.C. Part of the work used the UCSD-MTI Battery Fabrication Facility and the UCSD-Arbin Battery Testing Facility. Electron microscopic characterization was performed at the San Diego Nanotechnology Infrastructure (SDNI) of UCSD, a member of the National Nanotechnology Coordinated Infrastructure, which is supported by the National Science Foundation (grant ECCS-1542148). Computational support for this work was provided by the National Energy Research Scientific Computing Center (NERSC), a US Department of Energy Office of Science User Facility operated under contract no. DE-AC02-05CH11231. This work also used the Extreme Science and Engineering Discovery Environment (XSEDE)[53] on the Comet supercomputer at the San Diego

Supercomputing Center, which is supported by National Science Foundation grant no. ACI-1548562.

Author contributions

J.H. conceived the original idea. P.L. and Z.C. directed the project. J.H., H.L. and Z.W. carried out the experiments. Z.W., X.X., S.Y., G.C. and Y.Y. assisted with characterization. T.A.P. directed the computational experiments. J.H., H.L., Z.C. and P.L. wrote the paper. All authors discussed the results and commented on the manuscript.

Competing interests

The authors declare no competing interests.

Additional information

Supplementary information The online version contains supplementary material available at https://doi.org/10.1038/s41560-021-00783-z.

Correspondence and requests for materials should be addressed to T.A.P., Z.C. or P.L.

Peer review information *Nature Energy* thanks Kevin Leung and the other, anonymous, reviewer(s) for their contribution to the peer review of this work.

Reprints and permissions information is available at www.nature.com/reprints.

Publisher's note Springer Nature remains neutral with regard to jurisdictional claims in published maps and institutional affiliations.